control devices at 6 GHz under a steady temperature of 25°C. The main reason for the selection of 25°C that it is more stable for obtaining the signal data than the other temperatures such as 22–24°C. When one antenna port (Tx1) is transmitting, the other antenna port (Rx5) is receiving. Here, the Rx5 port in the 8 port antennas with circular structure is the farthest distance from the Tx1 port at 150 mm. In this process, the amplitude and phase of the signal can be obtained in the time domain. In Figure 3, we can observe a temperature influence on the matching liquid in the tank filled with 13BG. When temperature control devices are used in the platform system, the temperature of the matching liquid is maintained at a constant. The measured data can be used to obtain a stable value. Thus, we can utilize the stable signal data not only for the image reconstruction of a small object but also for the performance verification of the measured data in the frequency domain. If temperature control devices are not used, the signal data shows a downward flow tendency for a temperature variation of 1.1°C. This tendency is shown for both the amplitude (with the peak to peak deviation of 1.311 dB for 1.1°C) and the phase (with the peak to peak deviation of 14.53 degrees for 1.1°C). For both the amplitude and the phase, the zero (number) is based on the first value of the measured data. The consecutive values (number) after the first value are obtained from different by subtracting the consecutive values from the first value.

Figure 4 shows the time domain results of 13BG according to the frequency change from 3 to 6 GHz while a maintaining temperature of 25°C. As shown in Figure 4, the measured amplitude and phase confirmed the stable value for the entire frequency range under a constant temperature of the matching liquid.

The peak to peak deviation of the amplitude and phase is approximately 0.117 dB and 3.68 degrees. To minimize the peak to peak deviation of the signal, the enhanced MT system aimed for image reconstruction of small object will be implemented and the results will be analyzed.

3. CONCLUSION

We have analyzed the temperature influence of the matching liquid in the MT platform system operating in the frequency range of 3–6 GHz. The temperature variation of the matching liquid in the platform system is the important factor for the image reconstruction aimed for breast cancer detection. It was found that temperature control devices are required in the MT system to obtain the stable measurement data. Further work is necessary to investigate the detailed temperature characteristics of the matching liquid.

ACKNOWLEDGMENTS

This research was funded by the MSIP (Ministry of Science, ICT & Future Planning), Korea in the ICT R&D Program 2014.

REFERENCES

1. A. A. Bakar, A. Abbosh, P. Sharpe, M. E. Bialkowski, and Y. Wang, Heterogeneous breast phantom for ultra wideband microwave imaging, Microwave Opt Technol Lett 53 (2011), 1595–1598.
2. J. M. Sil, E. C. Fear, Tissue sensing adaptive radar for breast cancer detection–experimental investigation of simple tumor models, IEEE Trans Microwave Theory Tech 53 (2005), 3312–3319.
3. E. J. Bond, X. Li, S. C. Hagness, and B. D. Van Veen, Microwave imaging via space-tme beamforming for early detection of breast cancer, IEEE Trans Antennas Propag 51 (2003), 1690–1705.
4. P. M. Meaney, M. W. Fanning, D. Li, S. P. Pop-lack, and K. D. Paulsen, A clinical prototype for active microwave imaging og the breast, IEEE Trans Microwave Theory Tech 48 (2000), 1841–1853.
5. S. H. Son, N. Simonov, H. J. Kim, J. M. Lee, and S. I. Jeon, Preclinical prototype development of a microwave tomography system for breast cancer detection, ETRI J 32 (2010), 901–910.
6. P. Kosmas, C. M. Rappaport, and E. Bishop, Modeling with the FDTD method for microwave breast cancer detection, IEEE Trans Microwave Theory Tech 52 (2004), 1890–1897.
7. J. M. Sill and E. C. Fear, Tissue sensing adaptive radar for breast cancer detection: Study of immersion liquids, Electron Lett 41 (2005), 113–115.
8. P. Meaney, K. D. Paulsen, B. W. Pogue, and M. I. Miga, Microwave image reconstruction utilizing log-magnitude and unwarpped phase to improve high-contrast object recovery, IEEE Trans Medical Imag 20 (2001), 104–116.
9. N. Simonov, S. I. Jeon, S. H. Son, J. M. Lee, and H. J. Kim, 3D microwave breast imaging based on multistatic radar concept system, J Electromagn Eng Sci 12 (2012), 107–114.
10. C. A. Balanis, Advanced engineering electromagnetics, Wiley, New York, 1989.
11. C. Rønne, L. Thrane, P. O. Åstrand, A. Wallqvist, K. V. Mikkelsen, and S. R. Keiding, Investigation of the temperature dependence of dielectric relaxation in liquid water by THz reflection spectroscopy and molecular dynamics simulation, J Chem Phys 107 (1997), 5319–5331.

A FABRY–PEROT SENSOR PROTOTYPE FOR LOW-PRESSURE MEASUREMENTS

P. Roriz,[1,2] M. S. Ferreira,[1] K. Schuster,[3] J. Kobelke,[3] and O. Frazão[1]

[1] INESC-Porto and Faculty of Sciences of the University of Porto (FCUP), Porto, Portugal
[2] Instituto Superior da Maia (ISMAI), Maia, Portugal
[3] Leibniz Institute of Photonic Technology, Albert-Einstein-Str. 9, 07745, Jena, Germany

Received 13 May 2014

ABSTRACT: *An interferometric Fabry–Perot cavity based on hollow-core ring photonic crystal fiber combined with a silicone diaphragm is proposed for low pressure sensing. The sensor exhibits a sensitivity of 0.086 nm/mmHg for a pressure range between 0 and 337.5 mmHg. These values are in the range of physiological pressures, such as intravascular pressure.* © 2014 Wiley Periodicals, Inc. Microwave Opt Technol Lett 56:2981–2984, 2014; View this article online at wileyonlinelibrary.com. DOI 10.1002/mop.28749

Key words: *Fabry–Perot sensor; blood pressure; biomechanics*

1. INTRODUCTION

The most common working principles used with fiber optic sensors for biomedical and biomechanical research are based on intensity, phase, and wavelength modulation. Earlier intensity modulation schemes, based on glass fibers bundles, were reported in the 1960s [1,2]. Nowadays, they are easy to interrogate and probably also the most widespread [3]. Commercial sensors are already being used for a wide range of physiological pressure measurements [4–6]. Wavelength modulation is typically achieved through the use of fiber Bragg grating sensors which are highly recommended for temperature and/or strain measurements [7,8]. Most usual applications are with bone tissue [9,10] and dental cements [11,12]. Interferometric sensors, particularly those based on the Fabry–Perot (FP) configuration,

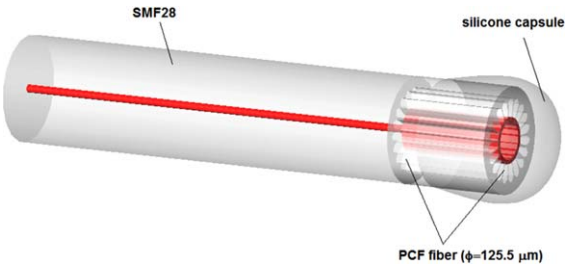

Figure 1 Schematic drawing of the FP pressure prototype. [Color figure can be viewed in the online issue, which is available at wileyonlinelibrary.com]

are also becoming interesting for biomechanical and biomedical research [13]. They have been introduced in the early 1980s [14,15] and compared to the previous modulation schemes are capable to attain higher sensitivity and resolution [13,16]. A sensing head based on FP cavity for pressure measurement is usually made by an air cavity and two parallel reflecting surfaces at the ends. A hollow-core fiber forms the optical cavity, which is spliced to a standard optical fiber at one end and to a movable diaphragm at the opposite end [17]. Pressure makes the diaphragm to change the optical cavity depth, where multiple reflections occur, causing a phase shift in the original spectrum [13]. The presence of the diaphragm seems mandatory for pressure measurements of liquids [18–20] while a diaphragm-free topology is possible for sensing gases pressures [21,22].

In this study, an interferometric FP cavity based on hollow-core ring photonic crystal fiber (HCR-PCF) combined with a silicone diaphragm is proposed for low-pressure sensing.

2. EXPERIMENTAL SETUP AND RESULTS

The sensor head consisted of an air cavity provided by a HCR-PCF and the reflecting surfaces of a standard single mode fiber (SMF28) and of a biocompatible silicone diaphragm (Fig. 1). The HCR-PCF has an outer diameter of 125.5 μm, a large hollow core, with a diameter of 44.4 μm, and several petal shaped holes with an azimuthal diameter of 24.4 μm [22]. In between these two structures, there is a 3.1-μm-thick silica ring [22]. The optical device fabrication included three main steps: first, the splice between the SMF28 and the HCR-PCF is made. The SMF28 provides the incoming light from the light source and the first reflecting surface. The splice was performed with a commercial arc fusion splicer mainly in the SMF28 region avoiding collapse of the HCR-PCF holes [23]. The second step includes cleaving the opposite end of the HCR-PCF near the splice to obtain a cavity length in the order of the fiber diameter

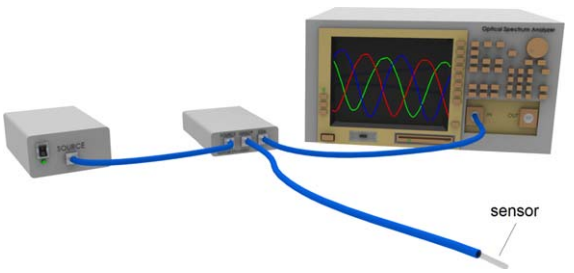

Figure 2 Schematic drawing of the interrogation setup used. An optical circulator connects the source to the sensor and the sensor to the optical spectrum analyzer. [Color figure can be viewed in the online issue, which is available at wileyonlinelibrary.com]

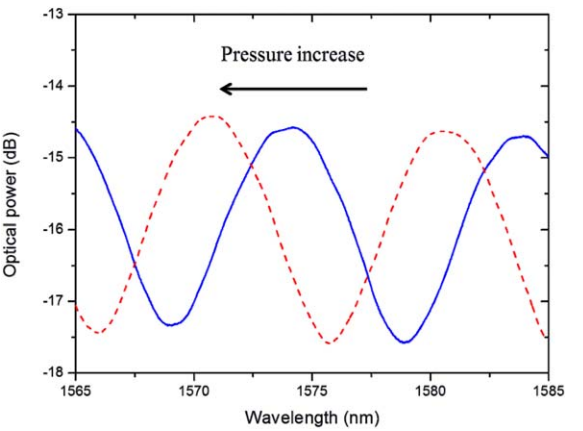

Figure 3 The spectral response of the sensing head. A phase shift caused by the increase of pressure can also be observed. [Color figure can be viewed in the online issue, which is available at wileyonlinelibrary.com]

or smaller. In fact, the spectral response depends on the FP cavity length [17]. In this study, the cavity length was maintained similar the outer diameter of the HCR-PCF. Finally, a silicone diaphragm was fabricated at the opposite end of the HCR-PCF. A biocompatible silicone polymer (Silastic Medical Adhesive Silicone, Type A, Dow Corning) was used. The diaphragm was obtained through repeated and controlled contact of the PCF-HCR tip with a small portion of silicone. With this process is not possible to completely control diaphragm geometry, which also affects the spectral response [24]. After a 72 h curing time (room temperature), the sensor was tested. The optical cavity is formed when light travelling from the SMF28 excites the HCR-PCF ring. Afterward, light is reflected due to the HCR-PCF end face cleavage and the silicone capsule, and recoupled to the SMF28. Under pressure the silicone diaphragm is compressed and a phase shift change is observed. The acquisition system consisted of a broadband light source centered at 1570 nm with a bandwidth of 100 nm and an optical circulator with three ports to measure the reflection signal of the FP. An optical spectrum analyzer is used to read the spectral response of the sensing head (Fig. 2).

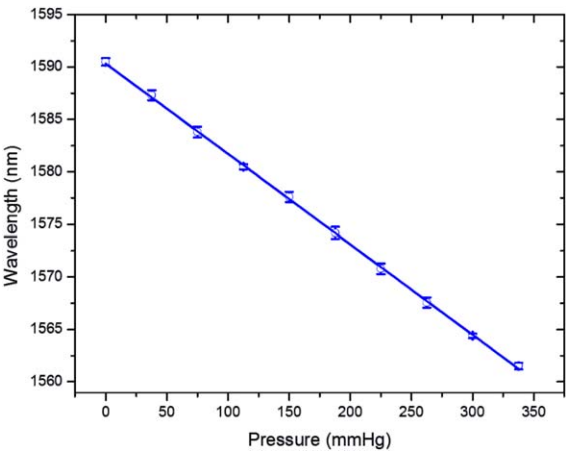

Figure 4 Mean wavelength shift versus pressure variation of the sensing head. The *y*-error bars represent the standard deviation. [Color figure can be viewed in the online issue, which is available at wileyonlinelibrary.com]

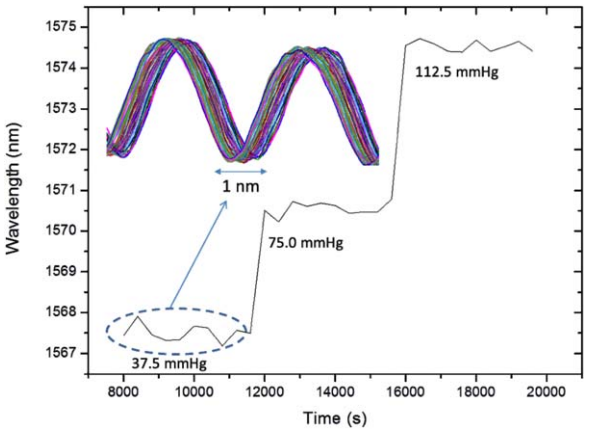

Figure 5 Typical shift of the sensor for a 60 min period under constant pressure. [Color figure can be viewed in the online issue, which is available at wileyonlinelibrary.com]

The sensor was characterized for hydrostatic pressure using a purpose-built pressure device that was described elsewhere [25]. Six pressure cycles from 0 to 337.5 mmHg with a pressure step of ~37.5 mmHg were performed.These presures are in the range of several physiological pressures, such as blood pressure, intracranial, and intra-articular pressures. The spectral response of the sensor is exhibited in Figure 3.

The cavity length (L) was estimated using the following equation: $\Delta L = \lambda^2/(2n\Delta\lambda)$, where λ is the operation wavelength, $\Delta\lambda$ corresponds to the signal period and n is the refractive index of the air. The value obtained for the optical cavity was ~125 μm. In Figure 4, the average results of the six pressure cycles are presented. Figure 5 shows typical shift of the sensor under constant pressure.

The sensing head presented a linear response ($r^2 = 0.9997$) with a pressure sensitivity of −86 pm/mmHg. In this case, a negative response was observed. Usually, when pressure is applied to a FP cavity two behaviors are expected: one induced by the photo-elastic effect; the other by the variation in the cavity length. In this case, the negative response of the sensing head arises from the variation of cavity length. The output signal difference between two consecutive steps of pressure (ΔP) were determined. On average, these wavelength differences ($\Delta\lambda$) were of 3.22 ± 0.24 nm. The mean standard deviation ($\delta\lambda$) of each step of calibration was 0.31 ± 0.12 nm, which represents approximately 9.7% of the average difference between consecutive steps of calibration. Maximum hysteresis was of 1.14 nm representing 3.6% of full scale output (FSO). The sensor resolution was calculated using the equation: $r = 2\delta\lambda\Delta P/\Delta\lambda$. The value obtained for the resolution was 22.6 mmHg representing about 7% of FSO. Maximum sensor drift during a measurement period of 60 min was approximately 1.0 nm. This variation could be explained by small variations around ambient temperature. Typically, silicone thermal expansion coefficient is $342.0 \times 10^{-6}/°C$, which is about 600 times higher than that of silica glass ($0.55 \times 10^{-6}/°C$).

3. CONCLUSION

A simple pressure sensor based on HCR-PCF and a silicone diaphragm was described. The sensor was tested for hydrostatic pressure and the pressures were in the range of some physiological pressures, such as blood pressure. It was obtained a good agreement between wavelength shift and pressure and with further optimization these type of sensor can be explored for ex vivo or in vivo measurements. Optimization should include control on the fabrication of the silicone diaphragm and sensor encapsulation (e.g., catheter or a spinal needle) to diminish the risk of sensor breaking and release of debris to the physiological medium.

ACKNOWLEDGMENTS

Project NORTE-07-0124-FEDER-000058 is financed by the North Portugal Regional Operational Programme (ON.2 – O Novo Norte), under the National Strategic Reference Framework (NSRF), through the European Regional Development Fund (ERDF), and by national funds, through the Portuguese funding agency, Fundação para a Ciência e a Tecnologia (FCT).

REFERENCES

1. M.L. Polanyi and R.M. Hehir, In vivo oximeter with fast dynamic response, Rev Sci Instrum 33 (1962), 1050–1054.
2. L.H. Lindström, Miniaturized pressure transducer intended for intravascular use, IEEE Trans Biomed Eng 17 (1970), 207–219.
3. P. Roriz, A. Ramos, J. Santos, and J. Simões, Fiber optic intensity-modulated sensors: A review in biomechanics, Photonic Sens 2 (2012), 315–330.
4. R.A. Pedowitz, D.H. Gershuni, A.G. Crenshaw, S.L. Petras, L.A. Danzig, and A.R. Hargens, Intraarticular pressure during continuous passive motion of the human knee, J Orthop Res 7 (1989), 530–537.
5. A.G. Crenshaw, J.R. Styf, S.J. Mubarak, and A.R. Hargens, A new transducer-tipped fiber optic catheter for measuring intramuscular pressures, J Orthop Res 8 (1990), 464–468.
6. M. Gelabert-Gonzalez, V. Ginesta-Galan, R. Sernamito-Garcia, A.G. Allut, J. Bandin-Dieguez, and R.M. Rumbo, The camino intracranial pressure device in clinical practice. Assessment in a 1000 cases, Acta Neurochir (Wien) 148 (2006), 435–441.
7. P. Roriz, L. Carvalho, O. Frazão, J.L. Santos, and J.A. Simões, From conventional sensors to fibre optic sensors for strain and force measurements in biomechanics applications: A review, J Biomech 47 (2014), 1251–1261.
8. H.J. Kalinowski, J.A. Simões, L. Carvalho, J.C. Silva, I. Abe, and M.S. Milczewski, Applications of fibre bragg grating sensors in biomechanics, In: International workshop on polymer optical fibers and international workshop on micro-structured polymer optical fibres, 2005, pp. 111–116.
9. T. Fresvig, P. Ludvigsen, H. Steen, and O. Reikerås, Fibre optic bragg grating sensors: An alternative method to strain gauges for measuring deformation in bone, Med Eng Phys 30 (2008), 104–108.
10. L. Carvalho, J.C. Silva, R.N. Nogueira, J.L. Pinto, H.J. Kalinowski, and J.A. Simões, Application of bragg grating sensors in dental biomechanics, J Strain Anal Eng 41 (2006), 411–416.
11. M.S. Milczewski, J.C. Silva, I. Abe, L. Carvalho, R.N. Nogueira, A.S. Paterno, H.J. Kalinowski, and J.L. Pinto, Determination of setting expansion of dental materials using fibre optical sensing, Meas Sci Technol 17 (2006), 1152–1156.
12. N. Alberto, L. Carvalho, H. Lima, P. Antunes, R. Nogueira, and J.L. Pinto, Characterization of different water/powder ratios of dental gypsum using fiber bragg grating sensors, Dent Mater J 30 (2011), 700–706.
13. P. Roriz, O. Frazão, A. Lobo-Ribeiro, J. Santos, and J. Simões, Review of fiber optic pressure sensors for biomedical and biomechanical applications, J Biomed Opt 18 (2013), 1–18.
14. S.J. Petuchowski, T.G. Giallorenzi, and S.K. Sheem, A sensitive fiber-optic fabry-pérot interferometer, IEEE J Quantum Electron 17 (1981), 2168–2170.
15. E. Cox and B. Jones, Fiber optic color sensors based on fabry-pérot interferometry, In: 1st international conference on optical fiber sensors, Inspec/IEE, 1983, pp. 122–126.
16. H.F. Taylor, Fiber optic sensors based upon the Fabry–Perot interferometer, In: F.T.S. Yu and Y. Shizhuo (Eds.), Fiber optic sensors, Marcel Dekker, New York, 2002, p. 509.
17. M.S. Ferreira, P. Roriz, S.O. Silva, J.L. Santos, and O. Frazão, Next generation of fabry-perot sensors for high-temperature, Opt Fiber Technol 19 (2013), 833–837.

18. S. Nesson, M. Yu, and A.H. Hsieh, A miniature fiber optic pressure sensor for intradiscal pressure measurements of rodents, In: Proceedings of SPIE 6528, 65280P, SPIE, 2007.
19. M.-D. Zhou, C. Yang, Z. Liu, J. Cysyk, and S.-Y. Zheng, An implantable Fabry-Pérot pressure sensor fabricated on left ventricular assist device for heart failure, Biomed Microdevices 14 (2012), 235–245.
20. R.A. Wolthuis, G.L. Mitchell, E.W. Saaski, J.C. Hartl, and M.A. Afromowitz, Development of medical pressure and temperature sensors employing optical spectrum modulation, IEEE Trans Biomed Eng 38 (1991), 974–981.
21. M.S. Ferreira, L. Coelho, K. Schuster, J. Kobelke, J.L. Santos, and O. Frazão, Fabry-Pérot cavity based on a diaphragm-free hollow-core silica tube, Opt Lett 36 (2011), 4029–4031.
22. M.S. Ferreira, J. Bierlich, H. Lehmann, K. Schuster, J. Kobelke, J.L. Santos, and O. Frazao, Fabry-Pérot cavity based on hollow-core ring photonic crystal fiber for pressure sensing, IEEE Photonics Technol Lett 24 (2012), 2122–2124.
23. O. Frazão, J.P. Carvalho, and H.M. Salgado, Low-loss splice in a microstructured fibre using a conventional fusion splicer, Microwave Opt Technol Lett 46 (2005), 172–174.
24. P. Roriz, O. Frazão, J.L. Santos, and J. Simões, Fiber optic sensors for physiological pressure measurements, In: VIII RIAO/XI OPTILAS, 2013.
25. P. Roriz, J.M.C. Ferreira, J.C. Potes, M.T. Oliveira, O. Frazão, J.L. Santos, and J.A.d.O. Simões, In vivo measurement of the pressure signal in the intervertebral disc of an anesthetized sheep, J Biomed Opt 19 (2014), 037006.

LOSS EFFECT ANALYSIS IN OPTICAL DELAY LINES BASED ON TWO COUPLED RESONATORS

Duykhanh Le, Thang Q. Tran, and Sangin Kim
Department of Electrical and Computer Engineering, Ajou University, Suwon, 443–749, Korea; Corresponding author:sangin@ajou.ac.kr

Received 13 May 2014

ABSTRACT: *A general analysis on loss effect on performances of coupled resonator-based optical delay lines is presented. Two types of the coupled resonators are considered: an electromagnetically induced transparency-like resonance and an all-pass filter. Our analysis reveals that the all-pass filter type is much more tolerant of the resonator loss.*
 Microwave Opt Technol Lett 56:2984–2987, 2014; View this article online at wileyonlinelibrary.com. DOI 10.1002/mop.28750

Key words: *coupled resonators; optical delay lines; loss analysis*

1. INTRODUCTION

Optical delay lines have important roles in optical communication systems and radio-frequency (RF) photonics. Especially, in forthcoming all-optical communication systems, variable optical delay lines are indispensable elements for the synchronization and the buffering of optical signals. RF-phased arrays for beam steering are another important application of the optical delay lines.

For the volume effectiveness of the optical delay lines, slowing down the speed of light is helpful. Recently, it has been shown that electromagnetically induced transparency (EIT), which originates from quantum interference of resonant pathways among atomic energy levels, can enormously slow down the speed of light [1,2]. Classical analogs of the EIT also have been demonstrated using optical resonators [3–6]. The optical resonator-based EIT-like phenomenon results from the interference of the decays of the resonators and it does not limited to specific types of resonators. Previously, it has been shown using the temporal coupled-mode theory that if two resonators are coupled via propagation channels such as a waveguide or free space, the EIT-like resonance of an arbitrarily narrow linewidth occurs within the resonant band of the single resonator, and the EIT-like resonant transmissions in two coupled slab waveguide gratings have been numerically demonstrated [7]. One of the advantages of the optical resonator-based EIT-like phenomenon is that its characteristics can be tuned in contrast to the EITs in atomic vapors [3,7] and thus, the variable optical delay lines can be implemented with it.

Another possible way to realize the optical delay lines based on the coupled resonators is an all-pass filter. In the coupled resonators, if the coupling via the propagation channel of a proper amount of phase retardation is balanced with evanescent coupling between the resonators, the all-pass filter is obtained [8]. An ideal characteristic of the all-pass filter is that its transmission is equal to 1 regardless of frequency and only group delay of signals arises from the dispersive behavior of the resonators.

In the EIT-like phenomenon and the all-pass filter based on optical resonators, losses of the resonators affect their performances. In addition to obvious overall signal power reduction, the losses affect group delay values. So far, not much attention has been paid to the effect of the loss in optical delay line applications of the optical resonators. In this work, we theoretically analyze the loss effect on the performances of the two optical delay line schemes based on the coupled resonators. In particular, we focus on coupled slab waveguide grating systems and derive the loss requirement for the optical delay line applications.

2. THEORY

Figures 1(a) and 1(b) show a general two coupled resonator structure and its example implementation composed of slab waveguide gratings, respectively. In general, the wave propagation channel in Figure 1(a) can be a waveguide or free space, and it corresponds to the free space in the case of the coupled gratings depicted in Figure 1(b). The coupling of resonators via propagation channel is characterized by a field decay rate, $1/\tau$ and a phase retardation, θ. The decay rate of the grating is related to a quality factor of its guided-mode resonance, that is, $Q=\omega_o\tau/4$, where ω_o is a resonance frequency. Note that $1/\tau$ is a decay rate in one direction. When two resonators are placed close to each other, evanescent coupling also should be considered, which can be quantified by an overlap integral of two guided modes in the grating system as depicted in Figure 1(b).

The temporal change of the normalized mode amplitudes of the resonators, a_1 and a_2 are described by [7,9]

$$\frac{da_1}{dt}=\left(j\omega_o-\frac{1}{\tau_L}-\frac{2}{\tau}\right)a_1-j\mu a_2+\kappa s_{+1}+\kappa s_{+2}, \tag{1a}$$

$$\frac{da_2}{dt}=\left(j\omega_o-\frac{1}{\tau_L}-\frac{2}{\tau}\right)a_2-j\mu a_1+\kappa s_{+3}+\kappa s_{+4}, \tag{1b}$$

where $1/\tau_L$ is a field delay rate due to loss, μ is an evanescent coupling strength, and s_{+i} and s_{-i} are the amplitudes of the incoming and the outgoing waves, respectively. The complex mode amplitude, a is normalized such that $|a|^2$ is equal to the energy stored in the resonator, and the complex wave amplitude, s